

Adrian Szklarski¹, Robert Głębocki¹, Mariusz Jacewicz¹

Impact point prediction guidance parametric study for 155 mm rocket assisted artillery projectile with lateral thrusters

The modified configuration of the 155 mm rocket assisted projectile equipped with lateral thrusters was proposed. Six degree of freedom mathematical model was used to investigate the quality of the considered projectile. Impact point prediction guidance scheme intended for low control authority projectile was developed to minimize the dispersion radius. Simple point mass model was applied to calculate the impact point coordinates during the flight. Main motor time delay impact on range characteristics was investigated. Miss distance errors and Circular Error Probable for various lateral thruster total impulse were obtained. Monte-Carlo simulations proved that the impact point dispersion could be reduced significantly when the circular array of 15 solid propellant lateral thrusters was used. Single motor operation time was set to be 0.025 s. Finally, the warhead radii of destruction were analyzed.

1. Introduction

One of the most current tendencies in field artillery precision guided munition research area is to extend its range and apply the low-cost control mechanisms to reduce the existing collateral damage. The rocket-assisted projectile (RAP) is a kind of shell with a small solid propellant rocket engine at the base to increase its range [1]. The rocket motor ignites with some delay after muzzle exit, and operates for a short period of time to increase the flight velocity rapidly. After that, the

✉ Mariusz Jacewicz, e-mail: mjacewicz@meil.pw.edu.pl

¹Faculty of Power and Aeronautical Engineering, Warsaw University of Technology, Poland.
Emails: aszklarski@meil.pw.edu.pl, rglebocki@meil.pw.edu.pl



projectile flies as a standard unpowered artillery shell. In such a way, the range extension requirement could be fulfilled.

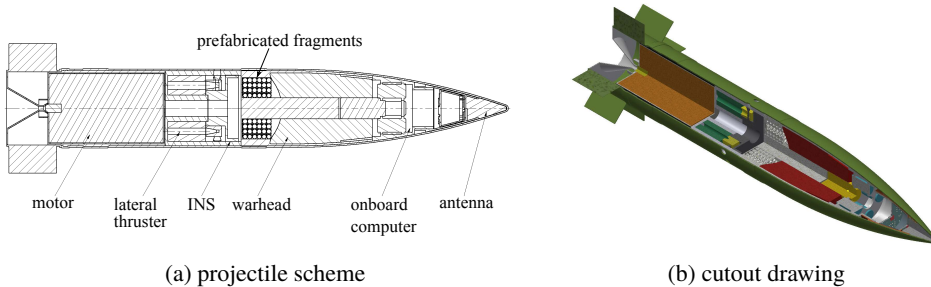
On the other hand, uncontrolled artillery munition is characterized by a significant dispersion, especially at the long ranges and at high gun elevation angles. There exists a lot of disturbances [2] which can create a significant dispersion of the impact points, e.g., muzzle velocity variations, tip-off effect or side wind. One of the current development tendencies aimed at improving the delivery accuracy is the use various correction systems, like body-fixed aero fins, roll decoupled canards, lateral thrusters, spin brakes, foldable plates or internal movable masses to reduce the collateral damage [3, 4]. In this way, the total number of fired shells could be decreased significantly. Low-cost solutions based on microelectromechanical systems could be used to realize this task. One of the most suitable method to control such relatively small projectiles is to use a set of solid propellant lateral thrusters. This kind of control is present on some existing guided munitions, e.g., STRIX mortar round or AccuLAR rocket artillery projectile. On the other hand, the second requirement is to extend the projectile range. An effective way to obtain this goal is to equip the shell with its own source of propulsion. For field artillery projectiles, lateral thruster control is less frequent, so there exists a need to investigate this type of control in detail.

The main problem with such a control system intended for a guided artillery munition is its low control authority due to the limited number of thrusters. The other issue is the pulsatile nature of work of this kind of systems. These types of control mechanisms are able to translate the rocket point of impact in the target plane only by several hundred meters. To overcome this difficulty, various control laws have been developed to date. The guidance approaches intended for precision guided munition could be divided into three main groups [4]: reference trajectory tracking, impact point prediction and trajectory shaping. The authors of [5] and [6] proposed a trajectory tracking guidance scheme based on pulse frequency modulation. The main disadvantage of this method is that a high thrust of the single thruster is required to realize the guidance process effectively. In [7], the trajectory tracking and proportional navigation were compared and it was concluded that the second one presents a poor performance in the vertical plane resulting from a trajectory curvature due to gravity. In [8], the modified linear theory was used successfully to reduce the munition dispersion significantly. In [9], the method of using pairs of impulse thrusters for spin-stabilized and fin-stabilized projectiles was investigated.

In the literature, there are scarce publications on the subject of rocket-assisted projectiles equipped with lateral thrusters. A variety of technical difficulties appear in such a sophisticated combined solution. The purpose of this paper was to develop the impact point prediction control law intended for RAP with single-use side thrusters-based control mechanism to achieve better dispersion reduction and to reduce its collateral damage.

2. Modified projectile configuration and control mechanism

The modified 155 mm artillery shell was proposed as a test platform for the purposes of this work. It was assumed that the projectile is equipped with a solid propellant rocket motor. The motor firing might be delayed by means of the inhibitor layer. The burnout gases fill the volume at the base of the projectile, reducing the base drag force and resulting in extended ranges. A set of 15 small, solid propellant lateral thrusters was added to achieve the controlled flight functionality (Fig. 1). These thrusters are spaced uniformly around the projectile body near the center of mass, because such a location ensures the lack of moment arm and quite a high control authority [10]. The nozzle of each of the motors is perpendicular to the shell longitudinal axis. By firing some of the thrusters, the shell is steered to the desired point. The main drawback of the proposed configuration is that each of the motors can be used only once. The control system includes also onboard computer, to calculate the prespecified control commands, and the strapdown Inertial Navigation System (INS) located in the projectile middle section to obtain an adequate velocity, angular rates, position and attitude.



(a) projectile scheme

(b) cutout drawing

Fig. 1. Proposed configuration of the modified 155 mm shell

The use of lateral thrusters on spin-stabilized projectiles is difficult because the time of operation of a single thruster should be less than 25% of the single revolution. To solve this problem, it was assumed that the shell is stabilized by a set of eight rectangular deployable fins to reduce the axis spin. The shell rotates clockwise (looking from base) due to small leading edges cant angles with maximum rate of $11000^{\circ}/s$ around the longitudinal axis during the flight. The main dimensions of the projectile are presented in Fig. 2.

Finally, using 3D CAD model, the shell mass and inertia parameters were obtained. Before the launch, they were assumed to be: the mass $m_0 = 45.5 \text{ kg}$, the moments of inertia $I_{x0} = 0.145 \text{ kgm}^2$, $I_{y0} = I_{z0} = 1.73 \text{ kgm}^2$ and the center of mass location (from the base) $x_{cg0} = 0.395 \text{ m}$. After main motor burnout, these parameters become: $m_k = 42.5 \text{ kg}$, $I_{xk} = 0.143 \text{ kgm}^2$, $I_{yk} = I_{zk} = 1.70 \text{ kgm}^2$, $x_{cgg} = 0.42 \text{ m}$.

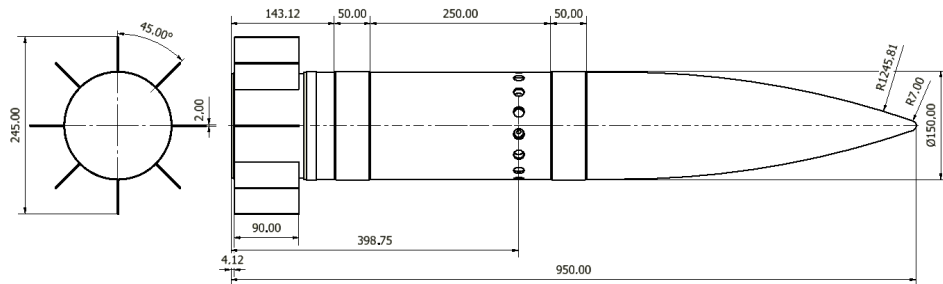


Fig. 2. Dimensions of the modified 155 mm shell (in millimeters)

2.1. Radius of destruction estimation

It was assumed that the shell is equipped with a fragmentation warhead composed of trinitrotoluene. Additionally, prefabricated fragments in the form of small steel circular balls are spaced equally behind the warhead to increase its effectiveness (Fig. 1). The radius of destruction R_{sk} of the shell was calculated as [11]

$$R_{sk} = \frac{\sqrt[3]{q}}{A \log e} \log \left(0.5D \sqrt{\frac{\alpha k_\varphi \sqrt[3]{q}}{E_{jsk}(2 - \alpha)}} \right), \quad (1)$$

where A is the empirical coefficient of the irregular shape (for spherical prefabricated fragment 0.029–0.03 $\frac{\sqrt[3]{kg}}{m}$). The parameter k_φ is the empirical coefficient for a fragment (here was assumed to be 0.00103 $\frac{Js^2}{cm^2 m^2 \sqrt[3]{g}}$). α is the coefficient of charging (the ratio between the mass of the charge and the total mass of the projectile) and its value is typically 15% for fragmentation warhead. E_{jsk} is the required unit effective energy of the fragment which, for eliminating the unprotected live force, was assumed to be 98 J/cm². D is the detonation velocity of explosive material (for TNT equals 6900 m/s), $e \approx 2.7182818$ is base of the natural logarithm. q is mass of the single fragment assumed equal to 3 g according to [12]. The diameter d of the single fragment was calculated as [11]

$$d = 2 \sqrt[3]{\frac{3q}{4\pi\rho_{steel}}}, \quad (2)$$

where ρ_{steel} is the density of the ball material (7800 kg/m³ for steel). The obtained fragment diameter is 9 mm. The radius of destruction of the projectile warhead at the impact point was calculated to be in the range from 64.5 m to 66.7 m, but for further calculations the worst case, smaller value was used.

3. Projectile flight dynamics model

To investigate the performance of the considered projectile configuration, the computer simulation was developed. Flat Earth approximation was used in the presented analysis. The projectile was modeled as a variable mass rigid body with six degrees of freedom (6DoF) and axial symmetry. Base drag variation due to main motor burn was included into the model. The shell equations of motion were derived in the body-fixed coordinate system $O_b x_b y_b z_b$ (Fig. 3).

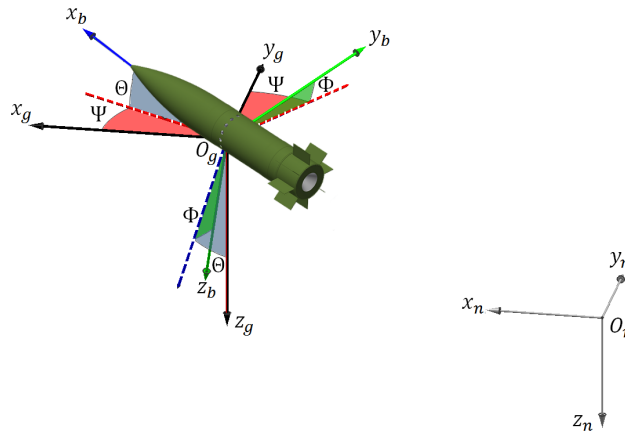


Fig. 3. Coordinate systems used in simulation

The 6DoF equation of motion of the projectile were [13–16]

$$\begin{bmatrix} \dot{U} \\ \dot{V} \\ \dot{W} \end{bmatrix} = \frac{1}{m} \begin{bmatrix} X_b \\ Y_b \\ Z_b \end{bmatrix} - \begin{bmatrix} 0 & -R & Q \\ R & 0 & -P \\ -Q & P & 0 \end{bmatrix} \begin{bmatrix} U \\ V \\ W \end{bmatrix}, \quad (3)$$

$$\begin{bmatrix} \dot{P} \\ \dot{Q} \\ \dot{R} \end{bmatrix} = \mathbf{I}^{-1} \begin{bmatrix} L_b \\ M_b \\ N_b \end{bmatrix} - \mathbf{I}^{-1} \begin{bmatrix} 0 & -R & Q \\ R & 0 & -P \\ -Q & P & 0 \end{bmatrix} \mathbf{I} \begin{bmatrix} P \\ Q \\ R \end{bmatrix}, \quad (4)$$

$$\begin{bmatrix} \dot{x}_n \\ \dot{y}_n \\ \dot{z}_n \end{bmatrix} = \begin{bmatrix} \cos \Theta \cos \Psi & \sin \Phi \sin \Theta \cos \Phi - \cos \Phi \sin \Theta & \cos \Phi \sin \Theta \cos \Phi + \sin \Phi \sin \Theta \\ \cos \Theta \sin \Psi & \sin \Phi \sin \Theta \sin \Phi + \cos \Phi \cos \Theta & \cos \Phi \sin \Theta \sin \Phi - \sin \Phi \cos \Theta \\ -\sin \Theta & \sin \Phi \cos \Theta & \cos \Phi \cos \Theta \end{bmatrix} \cdot \begin{bmatrix} U \\ V \\ W \end{bmatrix}, \quad (5)$$

$$\begin{bmatrix} \dot{\Phi} \\ \dot{\Theta} \\ \dot{\Psi} \end{bmatrix} = \begin{bmatrix} 1 & \sin \Phi \tan \Theta & \cos \Phi \tan \Theta \\ 0 & \cos \Phi & -\sin \Phi \\ 0 & \sin \Phi / \cos \Theta & \cos \Phi / \cos \Theta \end{bmatrix} \begin{bmatrix} P \\ Q \\ R \end{bmatrix}, \quad (6)$$

where U, V, W are projectile velocity components in body-fixed frame; P, Q, R are angular rates; x_n, y_n, z_n are position coordinates in inertial frame and Φ, Θ, Ψ are shell roll, pitch and yaw angles. The dot symbol above some variables denotes the first derivative with respect to time. m is the projectile mass and \mathbf{I} is the inertia matrix in the form

$$\mathbf{I} = \begin{bmatrix} I_x & 0 & 0 \\ 0 & I_y & 0 \\ 0 & 0 & I_z \end{bmatrix}. \quad (7)$$

The total forces \mathbf{F}_b and moments \mathbf{M}_b acting on the projectile were calculated as [17]

$$\mathbf{F}_b = \begin{bmatrix} X_b \\ Y_b \\ Z_b \end{bmatrix} = \mathbf{F}_g + \mathbf{F}_s + \mathbf{F}_a + \mathbf{F}_c, \quad (8)$$

where \mathbf{F}_g are gravity, \mathbf{F}_s propulsive, \mathbf{F}_a aerodynamic and \mathbf{F}_c control forces generated by lateral thrusters, respectively. In a similar way

$$\mathbf{M}_b = \begin{bmatrix} L_b \\ M_b \\ N_b \end{bmatrix} = \mathbf{M}_g + \mathbf{M}_s + \mathbf{M}_a + \mathbf{M}_c \quad (9)$$

are corresponding moments.

The gravity loads \mathbf{F}_g and \mathbf{M}_g in the body coordinate system $O_b x_b y_b z_b$ were calculated according to [13].

Main motor thrust misalignment was included into the model. The propulsive forces are [13]

$$\mathbf{F}_s = \begin{bmatrix} X_s \\ Y_s \\ Z_s \end{bmatrix} = T(t) \begin{bmatrix} \cos \Psi_T \cos \Theta_T \\ \cos \Theta_T \sin \Psi_T \\ -\sin \Theta_T \end{bmatrix}, \quad (10)$$

and the moments

$$\mathbf{M}_s = \begin{bmatrix} L_s \\ M_s \\ N_s \end{bmatrix} = \mathbf{r}_{cn} \times \mathbf{F}_s = T(t) \begin{bmatrix} 0 \\ -l_n \sin \Theta_T \\ -\cos \Theta_T \sin \Psi_T \end{bmatrix} \quad (11)$$

where $T(t)$ is the main motor thrust time history (Fig. 6b), Θ_T and Ψ_T are thrust pitch and yaw misalignment angles. l_n is the distance from center of mass to the

main motor nozzle exit plane. Using the data from [18], the propellant mass was assumed to be 3 kg and the total impulse 7593 Ns.

The aerodynamic force which acts on the projectile is

$$\mathbf{X}_a = \frac{1}{2} \rho V_0^2 S \begin{bmatrix} -C_X(\alpha, \beta, M, E_{\text{state}}) \\ C_Y(\alpha, \beta, M) \\ -C_Z(\alpha, \beta, M) \end{bmatrix} \quad (12)$$

and the aerodynamic moment is described by the formula

$$\mathbf{M}_a = \frac{1}{2} \rho V_0^2 S d \begin{bmatrix} C_L(\alpha, \beta, M) + C_{LP}(\alpha, \beta, M) \frac{Pd}{2V_0} \\ C_M(\alpha, \beta, M) + C_{MQ}(\alpha, \beta, M) \frac{Qd}{2V_0} \\ C_N(\alpha, \beta, M) + C_{NR}(\alpha, \beta, M) \frac{Rd}{2V_0} \end{bmatrix} \quad (13)$$

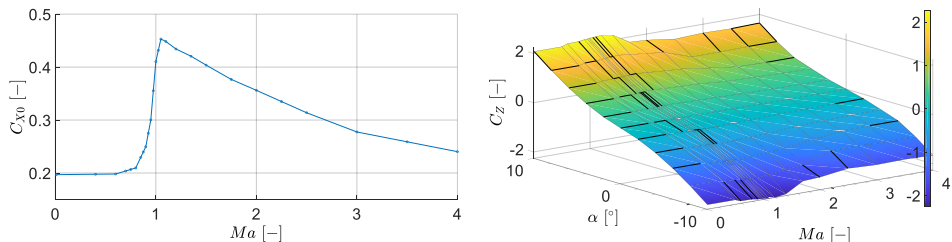
where ρ is the air density, V_0 is total aerodynamic velocity, $S = \pi d^2/4$ is the projectile fuselage largest cross section area and d is shell diameter. α is the angle of attack, β the angle of sideslip and M is Mach number. C_X , C_Y , C_Z are axial, side and normal force nondimensional coefficients. C_L is spin driving moment coefficient due to fin leading edge cant angles, and C_{LP} , C_{MQ} , C_{NR} are roll, pitch and yaw damping moment coefficients. E_{state} is the main motor state (0 – powered, 1 – unpowered flight). Aerodynamic coefficients were implemented into the software using the lookup table method.

The aerodynamic characteristics were calculated using semi-empirical engineering-level codes and analytical methods. The Magnus force and moment were neglected because they were small compared to other loads due to low spin rate of the projectile. The non-dimensional aerodynamic coefficients were assumed to be dependent on the angle of attack, the sideslip and the Mach number. In Fig. 4, the zero-yaw axial force and the normal force for zero sideslip angle coefficients are presented.

The interference effects between the lateral thruster and the flow field around the shell were neglected. The air thermodynamic properties were obtained using the US 76 Standard Atmospheric Model [19].

The control forces and moments were calculated as a sum of loads generated by individual side thrusters

$$\mathbf{F}_c = \sum_{j=1}^{15} \mathbf{F}_{Tj}, \quad \mathbf{M}_c = \sum_{j=1}^{15} \mathbf{M}_{Tj}. \quad (14)$$

(a) zero yaw axial force coefficient
(after main motor burnout)

(b) normal force coefficient

Fig. 4. Projectile aerodynamic coefficients

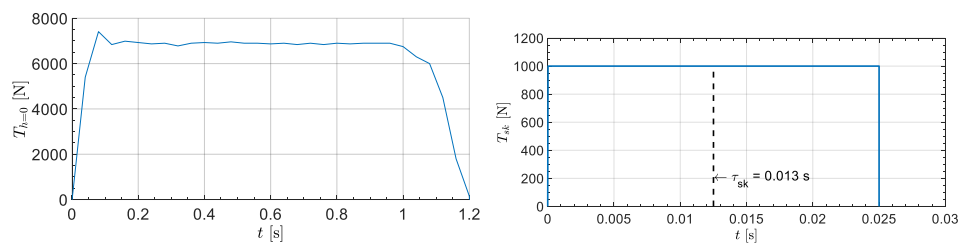
The force from j -th lateral thruster in the body fixed coordinate system $O_b x_b y_b z_b$ is

$$\mathbf{F}_{Tj} = T_{lt} \begin{bmatrix} 0 \\ \sin \Phi_j \\ \cos \Phi_j \end{bmatrix} \quad (15)$$

where T_{lt} is the thrust force of the thruster and Φ_j is angular location of the nozzle (Fig. 6b). The moments generated by the single lateral thruster are

$$\mathbf{M}_{Tj} = T_{lt} \begin{bmatrix} 0 \\ x_T \sin \Phi_j \\ x_T \cos \Phi_j \end{bmatrix} \quad (16)$$

where x_T is the distance from the shell center of mass to the plane including the lateral thrusters ring. The lateral thruster thrust curve was modeled as a trapezoidal pulse with the time duration of 0.025 s (Fig. 5b). Various thrust amplitudes between 200 N and 1000 N were considered.



(a) main motor

(b) lateral thruster

Fig. 5. Projectile rocket motors thrust curves

4. Impact point prediction guidance

It is assumed that the lateral thrusters are fired sequentially, according to Fig. 6a.

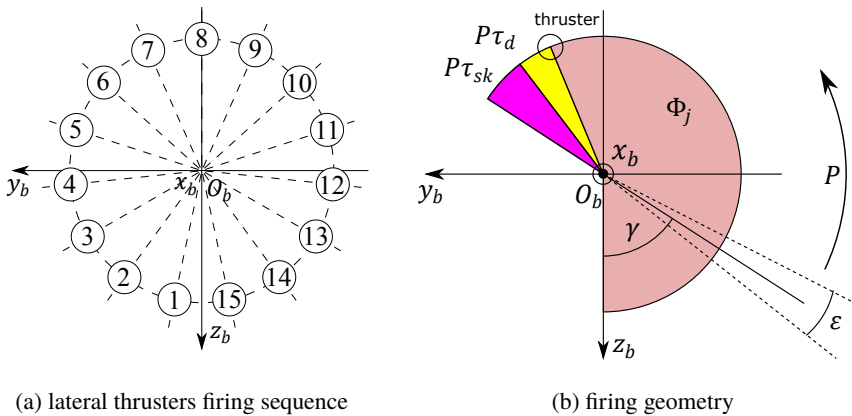


Fig. 6. Projectile lateral thrusters firing conditions (view from nose)

There exists a set of conditions to be defined when the single lateral thruster should be used [17]:

- the j -th lateral thruster has not been fired already
- the time from the previous motor firing is greater than t_{\min}

$$t \geq t_{\text{prev}} + t_{\min}, \quad (17)$$

where t is the current flight time, t_{prev} is the last moment in which one of the thrusters has been fired and t_{\min} is a threshold parameter which could be tuned during the flight.

- the thruster which should be fired is exactly on the opposite side of the fuselage with respect to the desired lateral projectile movement (Fig. 6b)

$$|\gamma - \Phi_j - \pi - P(\tau_d + \tau_{sk})| < \varepsilon, \quad (18)$$

Φ_j is the angle of the j -th lateral thruster, γ is the desired flight direction, P is the projectile roll rate, τ_d is the lateral thruster igniter delay and τ_{sk} is the half time of thruster burning time. ε is an angular activation threshold. The Φ_j angle is changed after each rocket firing. The time τ_{lt} was calculated as

$$\tau_{lt} = \frac{\int_0^{t_{lt}} T_{lt}(t) dt}{\int_0^{t_{lt}} T_{lt}(t) dt}, \quad (19)$$

where t_{lt} is the total burning time of the lateral thruster.

- the lateral thrusters are fired when the shell pitch angle is smaller than a pre-specified value and the time from launch is greater than t_g

$$\Theta \leq \Theta_g \quad \wedge \quad t \geq t_g. \quad (20)$$

Only 15 lateral thrusters firings are available, so it is not recommended to use them too early, for example immediately after launch, because in such a situation a lack of control authority might occur in the terminal phase of flight. The abovementioned constraint (20) allows for preventing from firing the thrusters too quickly.

The miss distance m_{dist} between the target location and the achieved point of impact in the target plane was calculated as

$$m_{\text{dist}} = \sqrt{(x_t - x_p)^2 + (y_t - y_p)^2}. \quad (21)$$

During the flight, this parameter is compared with the threshold value $m_{\text{dist}g}$. The correction is performed only when $m_{\text{dist}} \geq m_{\text{dist}g}$. The $m_{\text{dist}g}$ was chosen to be significantly smaller than the radius of destruction of the warhead. It was assumed that the target location coordinates x_t, y_t, z_t are known and implemented before the launch in the software of the onboard computer.

Various flight dynamics models could be used to predict the projectile impact point location during the flight [20, 21]. 6DoF models are numerically expensive, so the simplified analytical approaches have been developed. Projectile linear theory was described in [22] and [23], but is limited only to low launcher elevation angles. To overcome this drawback, the modified linear theory was extended to high elevation angles in [8] and [24]. The considered projectile spins slowly around the longitudinal axis, so it is assumed that the spin drift has a little influence on the shape of trajectory. It was decided that the point mass model would be suitable for the considered application. Only gravity and drag forces were included to the predictor model. The equations of motion in $O_n x_n y_n z_n$ coordinate frame used in the algorithm were as follows [20, 25, 26]

$$\ddot{x}_n = -\frac{\rho S C_{X0} V_0}{2m} \dot{x}_n, \quad (22)$$

$$\ddot{y}_n = -\frac{\rho S C_{X0} V_0}{2m} \dot{y}_n, \quad (23)$$

$$\ddot{z}_n = -\frac{\rho S C_{X0} V_0}{2m} \dot{z}_n + g. \quad (24)$$

The atmosphere thermodynamic properties were the same as those used in the 6DoF model. The axial force coefficient C_{X0} was parametrized using Mach number Ma . The main advantage of this model is its simplicity and short calculation time. No wind model was considered in the predictor. The main drawback of this approach is that the lateral motion due to projectile axial spin is neglected.

In the subsequent calculations, the initial conditions are obtained from the latest projectile state. Using the target coordinates x_t , y_t and predicted impact point location x_p , y_p , the longitudinal $x_p - x_t$ and lateral $y_p - y_t$ errors (Fig. 7) were calculated [27, 28]. The guidance correction kit was able to generate the control forces in the $O_b y_b z_b$ plane, so the transformation between errors in the horizontal target plane and the $O_b y_b z_b$ were provided [29, 30].

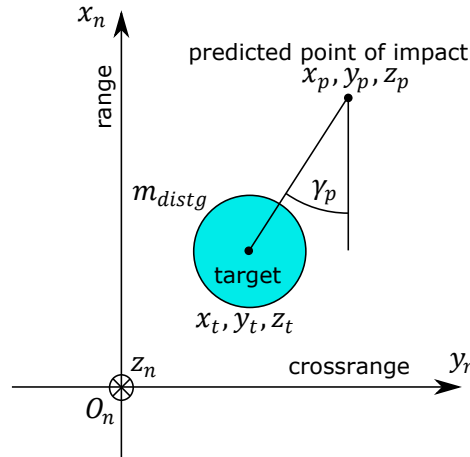


Fig. 7. Impact point location error

When the prediction errors in the target plane are known, the angle of correction $\gamma_p \in (0; 2\pi)$ is calculated as [23, 25, 28]

$$\gamma_p = \text{mod} \left(-\arctan 2 \frac{y_p - y_t}{x_p - x_t}, 2\pi \right). \quad (25)$$

5. Simulation results and discussion

The developed mathematical model was implemented into a MATLAB R2018a software. The equations of motion of the projectile were numerically integrated using the ode3 (Bogacki-Shampine) discrete step-solver with the step size 1e-4 s.

Firstly, the potential profit from the use of main motor was examined. To increase the range, the motor could be fired with some delay, so it was necessary to study the influence of this parameter on the achieved range. In the first case, unpowered flight was considered. For the subsequent simulation scenarios, the main motor was fired with various time delays $0 \leq t_d \leq 24$ with 4 s step. In this way, the optimum point at the trajectory of main motor firing was evaluated to extend the range. No lateral thrusters were fired in this part of simulations. The obtained shell axial velocity U time histories and trajectories in $O_n x_n y_n z_n$ frame are presented in Fig. 8.

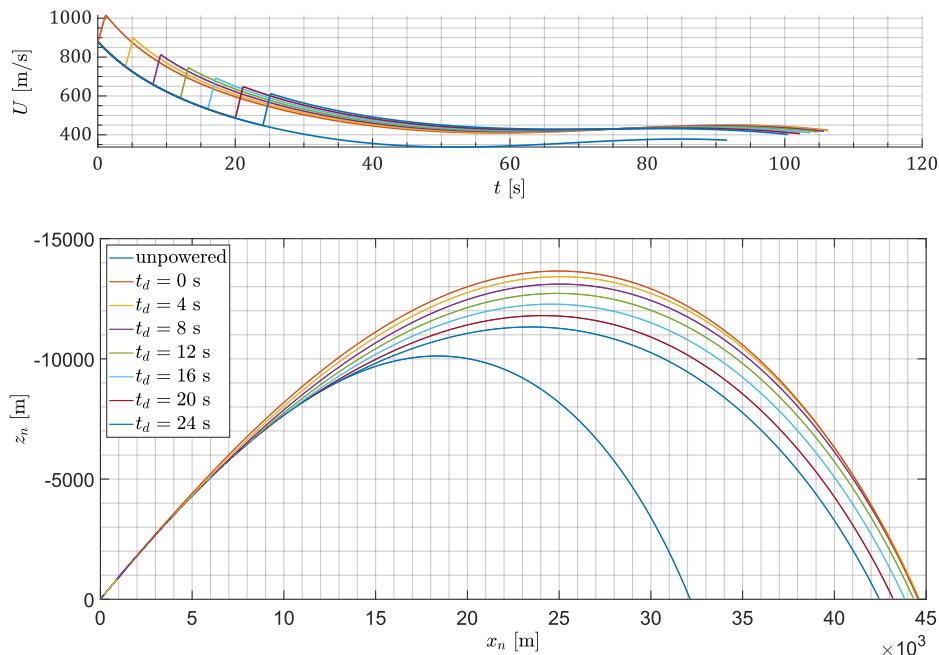


Fig. 8. Projectile flight parameters for various main motor firing delays

For the unpowered flight, the shortest range was obtained. After main rocket motor ignition, the projectile velocity increases rapidly. The RAP shell, having the same dimensions, has a longer range, higher vertex point and a longer time of flight.

Table 1.

Projectile range as a function of main motor ignition delay t_d

t_d [s]	Range [m]
Unpowered flight	32141.10
0	44563.73
4	44642.31
8	44588.05
12	44328.19
16	43848.53
20	43212.15
24	42453.34

The maximum range of 44642.31 m was achieved for the time delay $t_d = 4$ s. In this case, the range of the projectile was increased significantly with the help of main rocket motor when compared to unpowered flight.

Using the above results, the projectile footprint was calculated to evaluate the available projectile control authority. To realize this task, the series of simulations for $0 \leq \gamma \leq 360^\circ$ with step size 10° were evaluated. The thrusters were fired from the trajectory vertex up to the end of the flight with the time interval $t_{\min} = 0.5$ s. The angular tolerance of firing was set to $\varepsilon = 2.5^\circ$. The obtained trajectories are presented in Fig. 9 and the last phase of flight is visualized in Fig. 10. The black circles centered at the impact point of the unguided shell are equidistant lines with the interval of 100 m.

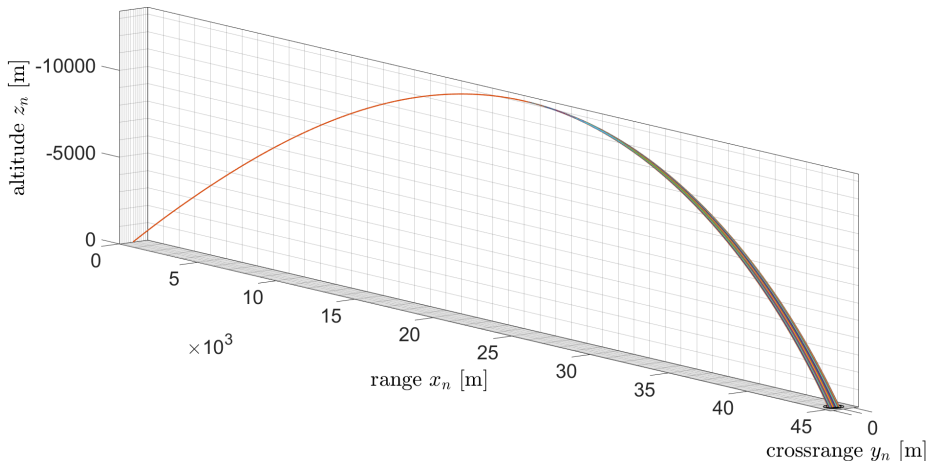


Fig. 9. Projectile trajectories

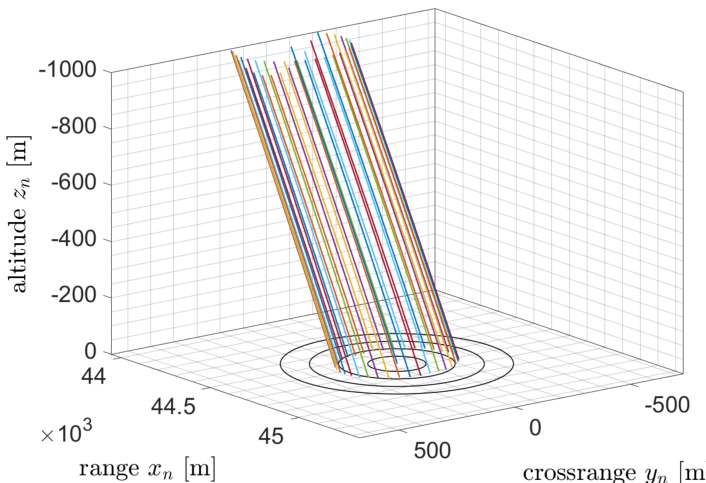


Fig. 10. Projectile footprint visualization

Next, the predictor convergence was analyzed. Single uncontrolled flight simulation for $t_d = 4$ s was run in such a manner that the miss distance at the end

of flight was zero. During this simulation, the impact point predictor was called with the frequency of 10 Hz during the whole flight and the equations (22)–(24) were integrated numerically using the variable-step ode45 method, but the lateral thrusters were deactivated. The “true” impact coordinates were known from 6DoF model, so it was possible to compare them with the predicted location of point of impact. The differences between the predicted impact points and target in the range $x_p - x_t$ and the cross-range $y_p - y_t$ were calculated and presented in Fig. 11.

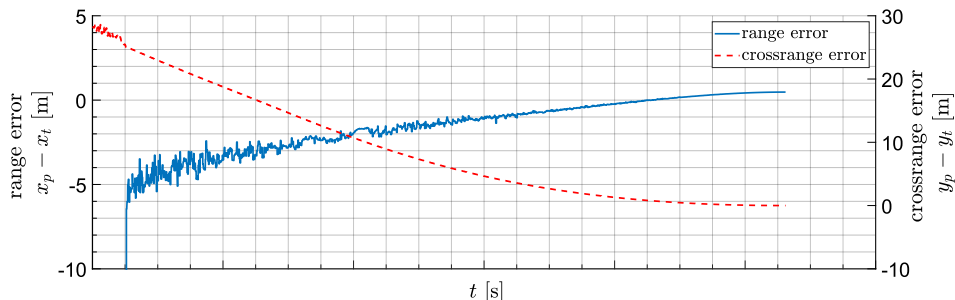


Fig. 11. Predictor convergence

The control process could be realized only when both of the errors have low value, for example smaller than 5 m. When one uses a perfect predictor, this error should be equal zero for the whole range of time, but on the other hand, such a highly accurate calculation requires a complicated model and is not necessary for practical purposes. At the beginning of flight, the range error is very high because no thrust force is included in the predictor, so it consequently works fine only for the unpowered phase of the flight. The cross-range error amplitude after 5 s is generally higher than for the range, because of neglecting the lateral drift due to projectile axial spin in Eqs. (22)–(24). Despite this fact, the cross-range error is under 10 m after 40 s of flight. Later, the absolute value of both errors decreases monotonically in time and, at the end of flight, is under 1 m.

Later, the influence of the lateral thruster force amplitude on the correctness of the guidance process was analyzed to initially obtain the most suitable total impulse I_{lt} of the propellant and to assess the maximum possible dispersion reduction. To achieve this goal, two kinds of trajectories were analyzed: a disturbed unguided, and a disturbed guided one (Table 2).

Six simulation scenarios were assumed and the amplitudes of the pulse were: 200 N, 400 N, 600 N, 800 N and 1000 N in subsequent cases, which corresponded to total impulses I_{lt} : 5 Ns, 10 Ns, 15 Ns, 20 Ns and 25 Ns. The stationary target was used in the considerations and its coordinates were 44.64 km in range and -0.28 km in cross range. The control system was activated after the trajectory vertex was reached, in the descending phase of flight, so $\Theta_g \leq 0^\circ$. The minimum time t_{\min} between two pulses was assumed to be 3 s. The visualization of the shell trajectories is shown in Fig. 12.

Table 2.
Shell initial launch parameters

Parameter	Nominal	Disturbed
Initial linear velocities	U_i [m/s]	32
	V_i [m/s]	1
	W_i [m/s]	1
Initial angular rates	P_i [$^{\circ}$ /s]	1356
	Q_i [$^{\circ}$ /s]	0
	R_i [$^{\circ}$ /s]	0
Initial attitude	Φ_i [$^{\circ}$]	0.0
	Θ_i [$^{\circ}$]	43
	Ψ_i [$^{\circ}$]	0
Main motor thrust misalignment	Θ_T [$^{\circ}$]	0
	Ψ_T [$^{\circ}$]	0
Mass and moments of inertia	m_i [kg]	45.5
	m_f [kg]	42.5
	I_{xi} [kgm ²]	0.145
	I_{xf} [kgm ²]	0.143
	$I_{yi} = I_{zi}$ [kgm ²]	1.73
	$I_{yf} = I_{zf}$ [kgm ²]	1.70

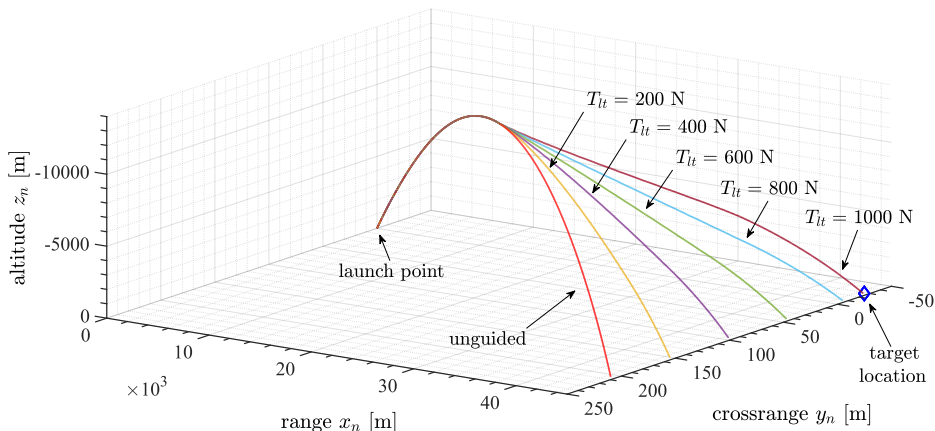


Fig. 12. Predictor trajectories

Fig. 13 and Fig. 14 present the projection of the shell trajectory in the guided phase on the horizontal $O_nx_ny_n$ and vertical $O_nx_nz_n$ planes.

When the guidance process starts, each of the trajectories are curved to the target. In the first three cases, the control force generated by an individual motor was too small to eliminate the miss distance. The most significant lateral correction

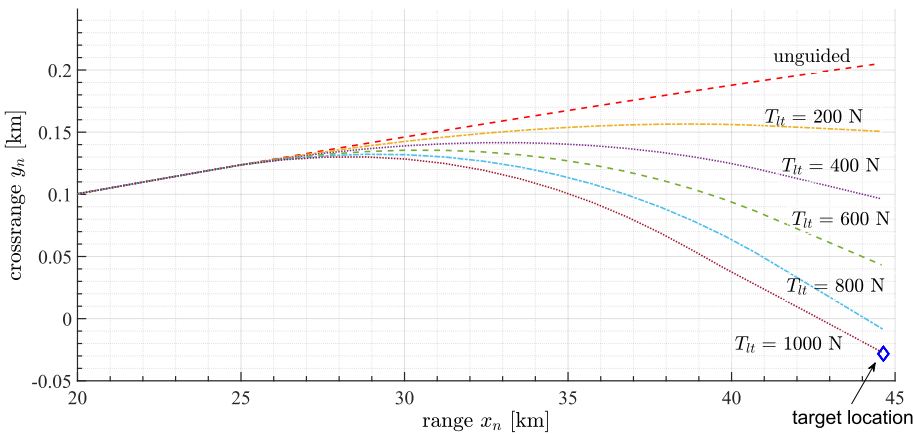


Fig. 13. The projectile trajectories in horizontal plane

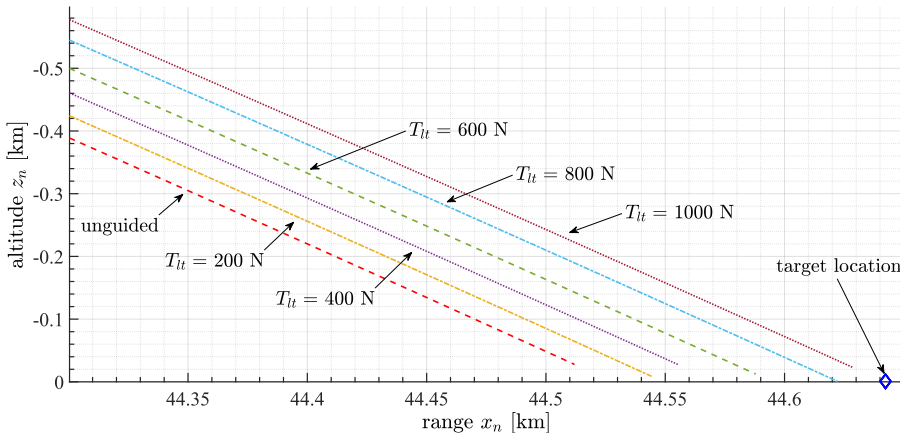


Fig. 14. Terminal phase of flight in vertical plane

capability was observed for the largest T_{lt} . The greatest range corrections were obtained in the last case, for the biggest T_{lt} . A small miss distance in range is observed in each case.

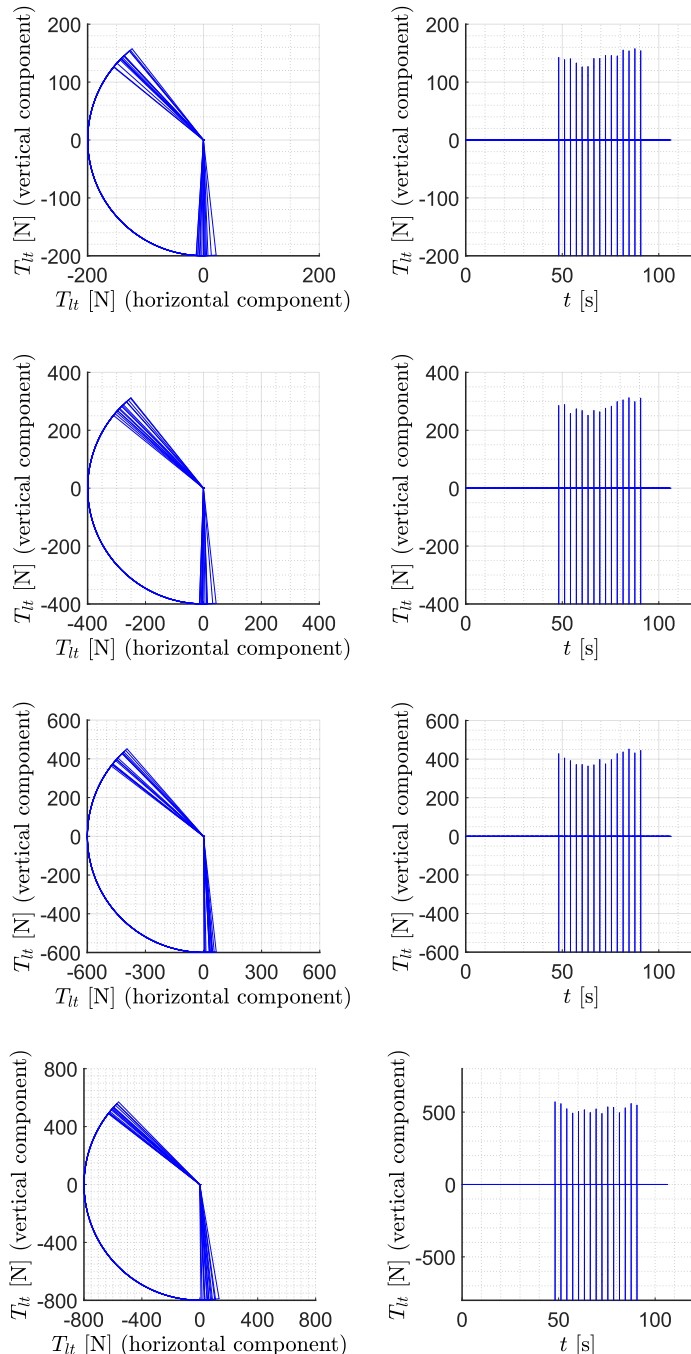
Table 3.

Miss distance variations for various lateral thrusters force amplitude

T_{lt} [N]	200	400	600	800	1000
m_{dist} [m]	201.5794	143.4550	85.5522	27.8893	0.7214

The miss distance decreases monotonically with the increase of the total impulse of the lateral thruster and takes the smallest value for $T_{lt} = 1000$ N. On the other hand, the reduction of the hit error exactly to zero is rather not required because of the warhead blast effect.

In Fig. 15, there are presented the forces generated by lateral thrusters in the plane perpendicular to the longitudinal axis of symmetry (view from the projectile base) and in vertical plane.



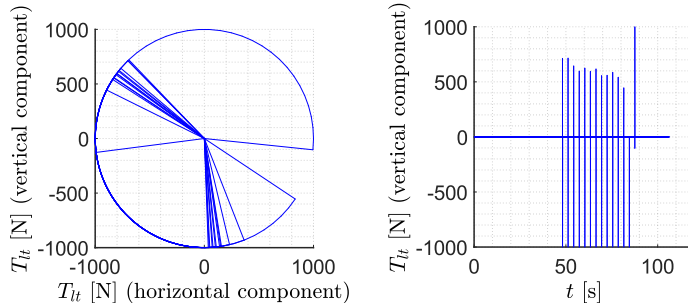


Fig. 15. Forces generated by the lateral thrusters

In each from the simulation scenarios, all the 15 thrusters were applied. In each case, a single thruster generates forces approximately by 1/3 of the roll cycle. The components of horizontal plane forces have mainly negative values, which means that the projectile is steered left looking from its base. The last 8 s of flight was unguided because of lack of the control authority.

The total angle of attack $\alpha_t = \tan^{-1} (\sqrt{V^2 + W^2}/U)$ was used to evaluate the influence of T_{lt} on dynamic behavior of the shell. The total angle of attack time histories are shown in Fig. 16.

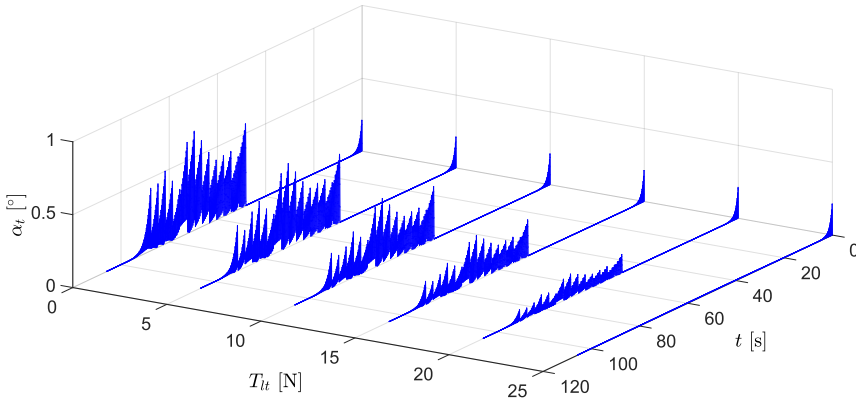


Fig. 16. The total angle of attack time histories

At the beginning of flight, small oscillations are observed due to the launch process. An amplitude increment occurs after each motor firing. The maximum value of the total angle of attack is achieved for the biggest thrust force and, in each case, it is smaller than 1° , which is an acceptable value for this kind of projectile.

The launch of the projectile was modeled as a random process. The Monte-Carlo simulation was used to investigate the shells dispersion and to assess the projectile accuracy and precision of the proposed guidance method. It was assumed

[17] that each of the disturbances separately could be described by a Gaussian distribution (Table 4). The Philox 4x32 algorithm was used to generate the pseudorandom input data. Standard deviations were assumed according to the data of similar projectiles [23, 30]. The calculations were performed on PC with IntelTM i7@3.6 GHz and 16 GB RAM.

Table 4.
Parameters for Monte-Carlo simulation

Parameter		Mean	Std. deviation
Initial linear velocities	U_i [m/s]	880	5
	V_i [m/s]	1	0.5
	W_i [m/s]	1	0.5
Initial angular rates	P_i [$^{\circ}$ /s]	1356	12
	Q_i [$^{\circ}$ /s]	0	1
	R_i [$^{\circ}$ /s]	0	1
Initial altitude	Φ_i [$^{\circ}$]	0.0	0.2
	Θ_i [$^{\circ}$]	43	0.1
	Ψ_i [$^{\circ}$]	0	0.1
Main motor thrust misalignment	Θ_T [$^{\circ}$]	0	0.01
	Ψ_T [$^{\circ}$]	0	0.01
Mass and moments of inertia	m_i [kg]	45.5	0.05
	m_f [kg]	42.5	0.05
	I_{xi} [kgm ²]	0.145	0.01
	I_{xf} [kgm ²]	0.143	0.01
	$I_{yi} = I_{zi}$ [kgm ²]	1.73	0.01
	$I_{yf} = I_{zf}$ [kgm ²]	1.70	0.01

Circular Error Probable (CEP) was used to compare the dispersion in both cases. CEP is a radius of the circle centered at the target that contains 50% of impact points. It was estimated as a median from radial miss distances.

To choose the best possible combination of guidance algorithm settings, a parametric study of on the model was performed. It was assumed that the main requirement was to achieve the CEP smaller than 5 m.

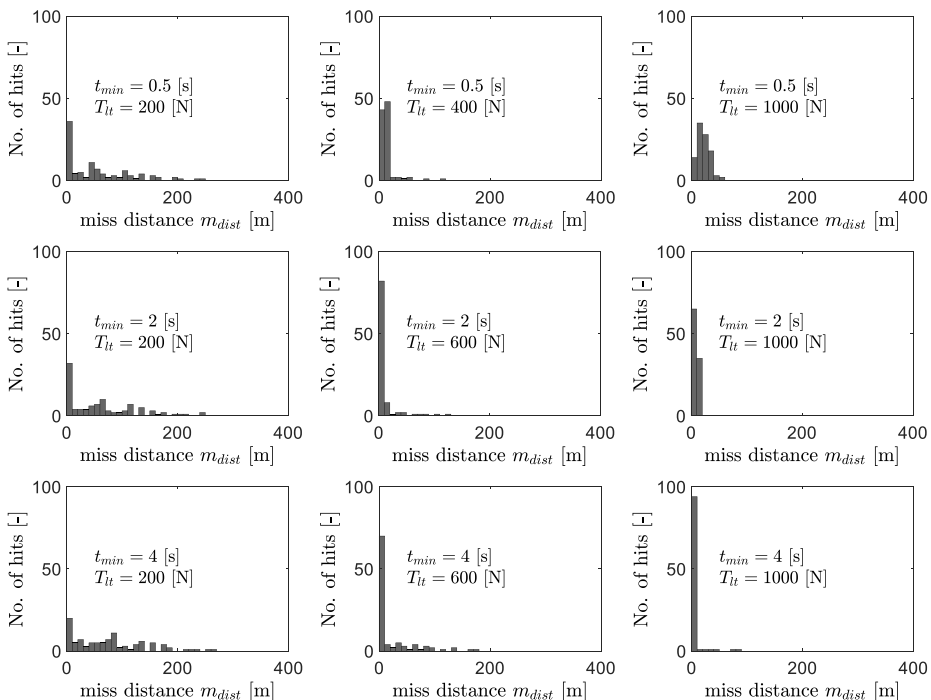
In order to evaluate the effect of minimum time that elapsed between two consecutive firings on the achieved CEP, a set of 100 Monte Carlo simulations was realized for various t_{\min} and lateral thruster thrust amplitudes T_{lt} . The resulting CEP was listed in Table 5. The miss distances for 200 N (small), 600 N (medium) and 1000 N (large lateral thrust) are visualized in Fig. 17 in the form of histograms. The size of the single bin was set to 10 m.

The smallest CEP was observed for $t_{\min} = 4$ s and $T_{lt} = 600$ N. The two minimal times between two consecutive pulses, 0.5 s and 1 s, are too small. For

Table 5.

CEP for various combinations of t_{\min} and T_{lt}

t_{\min} [s]	T_{lt} [N]				
	200	400	600	800	1000
0.5	43.18	10.18	11.36	14.58	20.13
1	44.51	7.59	8.67	11.11	12.49
2	50.23	4.92	6.11	8.12	7.62
3	58.07	3.37	3.20	3.72	2.78
4	69.93	2.69	0.85	0.93	1.03

Fig. 17. Miss distance histograms for various t_{\min}

$T_{lt} = 200$ N, an increase in t_{\min} results in a larger CEP. The accuracy requirement CEP < 5 m is fulfilled for T_{lt} equal to at least 400 N. In the most favorable situation, the miss distance histogram should be composed of a single bin at the left side of the graph, which corresponds to hit errors not bigger than several meters.

Next, the same methodology was used to assess the influence of Θ_g on the resulting CEP. The achieved results are presented in Table 6 and Fig. 18.

The CEP varies significantly in the subsequent cases, and its minimal value is obtained for $\Theta_g = -20^\circ$ and $T_{sk} = 800$ N. The thruster amplitude 200 N seems be too small to achieve the required accuracy. For $\Theta_g = -40^\circ$, a satisfactory

Table 6.
CEP for various combinations of Θ_g and T_{lt}

Θ_g [°]	T_{lt} [N]				
	200	400	600	800	1000
0	59.42	3.37	3.20	3.72	2.78
-10	68.65	20.80	2.03	2.75	2.29
-20	79.86	43.48	6.69	1.00	1.24
-30	91.64	66.98	42.56	18.13	1.50
-40	102.44	88.80	74.99	61.60	48.18

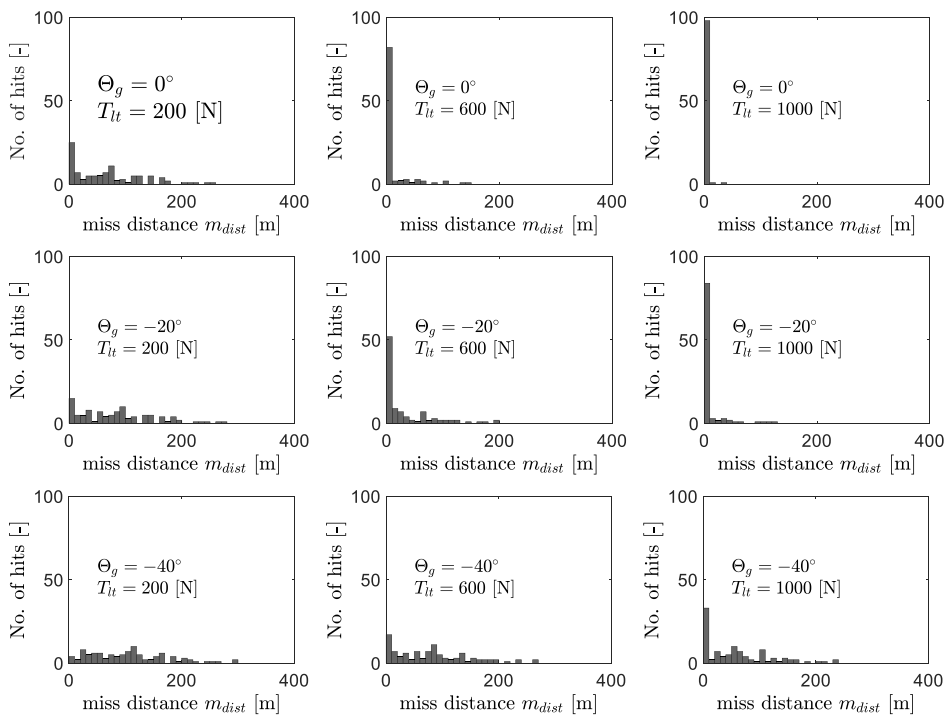


Fig. 18. Miss distance histograms for various Θ_g

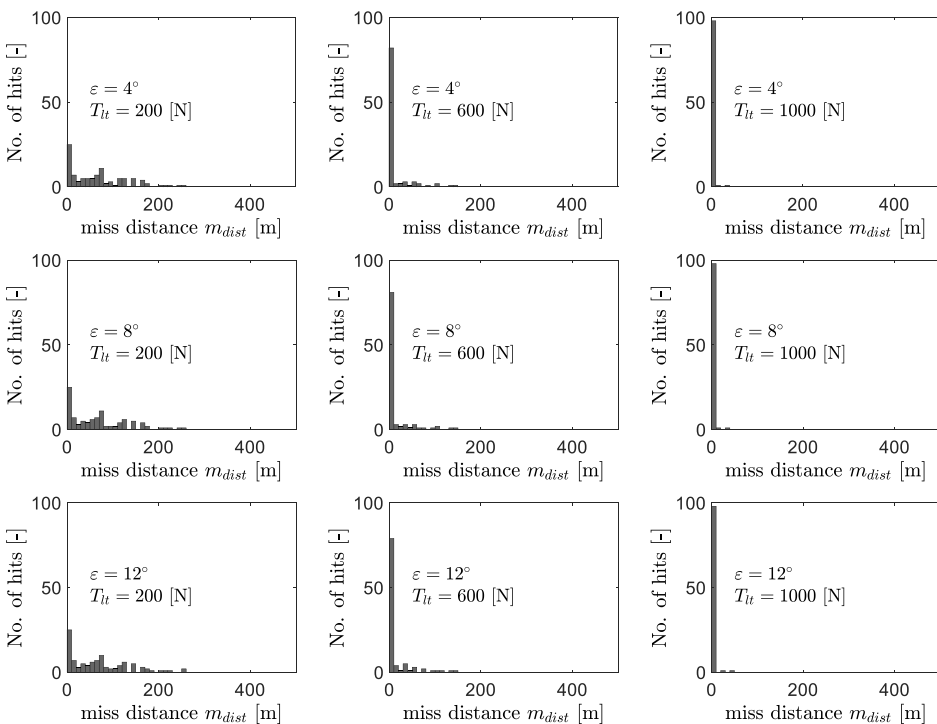
result wasn't achieved in any case, which means that is not appropriate to start the guidance process in the terminal phase of flight. When the guidance is initialized at trajectory vertex, the use of thrusters with thrust amplitude of at least 400 N makes it possible to obtain CEP not bigger than several meters.

In a similar way, in order to investigate the influence of ε on the resulting shell dispersion, a set of 100 Monte Carlo simulations was run for various parameter values. The following algorithm parameters were assumed: $t_{\min} = 3$ s, $\Theta_g = 0^\circ$ and $m_{\text{distg}} = 2$ m. The obtained CEP is presented in Table 7 and in Fig. 19.

Table 7.

CEP for various combinations of ε and T_{lt}

ε [°]	T_{lt} [N]				
	200	400	600	800	1000
4	59.421	3.3686	3.1972	3.7155	2.78
8	59.739	3.5917	2.8827	3.3896	2.67
12	60.425	4.378	2.3078	3.34	3.16

Fig. 19. Miss distance histograms for various ε

The results indicate that the CEP changes very little with the increase of ε . It means that the actual roll angle of the shell must be estimated with a precision of several degrees. The smallest CEP was achieved for $\varepsilon = 12^\circ$ and $T_{lt} = 600$. The accuracy requirements are met if the thrust amplitude is no smaller than 400 N.

Finally, the comparison between an unguided flight and guided flights with optimum parameters was evaluated for a larger statistic sample. One assumed $t_{\min} = 3$ s, $\Theta_g = 0^\circ$ and $\varepsilon = 4^\circ$. The number of simulations was set to 600 for each simulation scenario. The resulting hitting patterns are presented in Fig. 20, where the target coordinates are (0,0). The CEP is marked as a black circle. The green circles centered at each impact point are added to show the calculated radii

of destruction. The impact angles of the individual shells were similar, so it was assumed that the radii of destructions of all individual shells were equal.

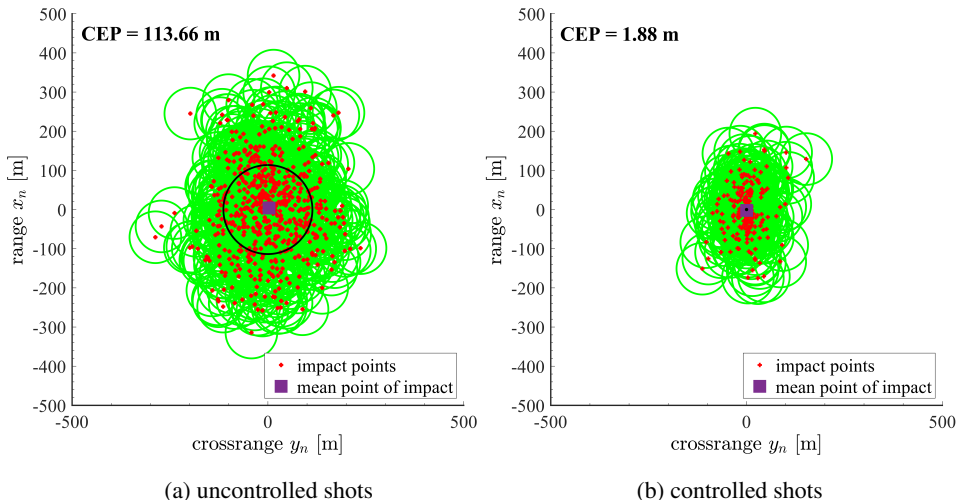


Fig. 20. Monte-Carlo hitting patterns

For guided projectiles, the impact points are much more concentrated around the target. The CEP for a controlled simulation scenario is 60.5 times smaller than in the ballistic case. The green area covered by explosion effects is also much smaller for guided flights, which means that the collateral damage effects are reduced significantly.

The histograms in Fig. 21 show comparison of miss distance between uncontrolled and guided flights.

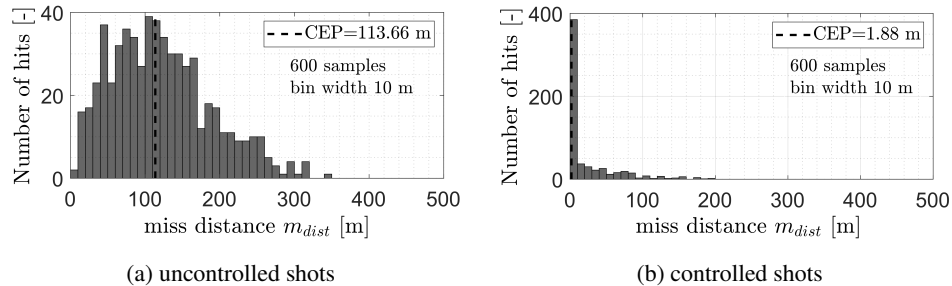


Fig. 21. Miss distance histograms

In the case of guided flight, 385 projectiles achieved miss distance smaller than 10 m. The maximum hit error didn't exceed 200 m. It shows that precision and accuracy of lateral thruster steered RAP are higher than of a standard unguided shell.

6. Conclusion

In this paper, a modified fin-stabilized 155 mm rocket-assisted projectile equipped with 15 solid-propellant lateral thrusters was proposed and investigated. Numerical simulations were performed to examine the efficiency of the guidance method. The use of rocket motor allows for extending the range approximately by 12.5 km. To achieve the maximum range, the main rocket motor should be fired with at least 4 s delay after the muzzle exit. The projectile control authority is 200 m when the lateral thrusters are used as a control mechanism. To overcome this difficulty and obtain functionality of the controlled flight, one developed prediction guidance of the impact point. It was found that, for a slow-spinning shell, the 3DoF point mass model makes it possible to realize the predictive guidance effectively when the control process starts in the terminal phase of flight. Assuming that the operation time of a single lateral thruster is 0.025 s, the total impulse should not be smaller than 5 Ns. The minimum time between two pulses should be in the interval from 2 s to 4 s. The hit accuracy depends strongly on the pitch angle threshold Θ_g and the optimum value of this parameter is between 0° and -20° . The most appropriate thrust amplitude should be in the range from 600 N to 1000 N. The CEP does not vary significantly with angular activation thresholds remaining between 4° and 12° . Monte-Carlo simulations indicated that, for a guided projectile, 60.5 times smaller dispersion could be observed, when compared to unguided shoots. It proves that the collateral damage could be reduced significantly when one applies the presented approach.

Manuscript received by Editorial Board, October 01, 2019;
final version, February 29, 2020.

References

- [1] Z. Guodong. The Study of the Modeling simulation for the Rocket-Assisted Cartridge. *IOP Conference Series Materials Science and Engineering*, 2018. doi: [10.1088/1757-899X/439/4/042038](https://doi.org/10.1088/1757-899X/439/4/042038).
- [2] F.R. Gantmakher and L.M. Levin. *The Flight of Uncontrolled Rockets*. Pergamon Press Ltd., 1964.
- [3] E. Gagnon and M. Lauzon. Low cost guidance and control solution for in-service unguided 155 mm artillery shell. Technical Report 2008-333, DRDC Valcaltier, Canada, 2009.
- [4] E. Gagnon and A. Vachon. Efficiency analysis of Canards-based course correction fuze for a 155-mm spin-stabilized projectile. *Journal of Aerospace Engineering*, 29(6):04016055, 2016. doi: [10.1061/\(ASCE\)AS.1943-5525.0000634](https://doi.org/10.1061/(ASCE)AS.1943-5525.0000634).
- [5] B. Pavkovic, M. Pavic, and D. Cuk. Frequency-modulated pulse-jet control of an artillery rocket. *Journal of Spacecraft and Rockets*, 49(2):286–294, 2012. doi: [10.2514/1.57432](https://doi.org/10.2514/1.57432).
- [6] B. Pavkovic, M. Pavic and D. Cuk. Enhancing the precision of artillery rockets using pulsejet control systems with active damping. *Scientific Technical Review*, 62(2):10–19, 2012.
- [7] T. Jitpraphai, B. Burchett, and M. Costello. A comparison of different guidance schemes for a direct fire rocket with a pulse jet control mechanism. *AIAA Atmospheric Flight Mechanics Conference and Exhibit*, Montreal, Canada, 6–9 August, 2001. doi: [10.2514/6.2001-4326](https://doi.org/10.2514/6.2001-4326).

- [8] N. Slegers. Model predictive control of a low speed munition. *AIAA Atmospheric Flight Mechanics Conference and Exhibit*. Hilton Head, South Carolina, 20-23 August, 2007. doi: [10.2514/6.2007-6583](https://doi.org/10.2514/6.2007-6583).
- [9] D. Corriveau, P. Wey, and C. Berner. Thrusters pairing guidelines for trajectory corrections of projectiles. *Journal of Guidance, Control, and Dynamics*, 34(4):1120–1128, 2011. doi: [10.2514/1.51811](https://doi.org/10.2514/1.51811).
- [10] D. Corriveau, C. Berner, and V. Fleck. Trajectory correction using impulse thrusters for conventional artillery projectiles. *Proceedings of 23rd International Symposium on Ballistics*, pages 639–646, Tarragona, Spain, 16-20 April, 2007.
- [11] C. Kwiecień. A concept of the air drag law for spherical fragments prepared on the basis of AASTP-1 allied publication data. *Issues of Armament Technology*, 146(2):73–91, 2018.
- [12] A. Faryński, A. Długołęcki and Z. Ziółkowski. Measurements of characteristics of warhead fragments of the 70-mm air-to-ground unguided missile. *Bulletin of the Military University of Technology*, 57(3):173–180, 2008 (in Polish).
- [13] *Military Handbook. Missile Flight Simulation. Part One. Surface-to-Air Missiles*. Department of Defense, USA, 1995.
- [14] F. Fresconi and M. Ilg. Model predictive control of agile projectiles. *AIAA Atmospheric Flight Mechanics Conference*, Minneapolis, USA, 13-16 August 2012. doi: [10.2514/6.2012-4860](https://doi.org/10.2514/6.2012-4860).
- [15] P. Lichota and J. Szulczyk. Output error method for tiltrotor unstable in hover. *Archive of Mechanical Engineering*, 64(1):23–36, 2017. doi: [10.1515/meceng-2017-0002](https://doi.org/10.1515/meceng-2017-0002).
- [16] P. Lichota, J. Szulczyk, M.B. Tischler, and T. Berger. Frequency responses identification from multi-axis maneuver with simultaneous multisine inputs. *Journal of Guidance, Control and Dynamics*, 42(11):2550–2556, 2019. doi: [10.2514/1.G004346](https://doi.org/10.2514/1.G004346).
- [17] T. Jitpraphai and M. Costello. Dispersion reduction of a direct-fire rocket using lateral pulse jets. *Journal of Spacecraft and Rockets*, 38(6):929–936, 2001. doi: [10.2514/2.3765](https://doi.org/10.2514/2.3765).
- [18] EDePro. 155 mm Hybrid Rocket Assist – Base Bleed Artillery Projectile [Online]. Available: www.edepro.com/files/RABB_catalogue.pdf [20 08 2019].
- [19] U.S. Standard Atmosphere. National Aeronautics and Space Administration, Washington, D.C., USA, 1976.
- [20] F. Fresconi, G. Cooper, and M. Costello. Practical assessment of real-time impact point estimators for smart weapons. *Journal of Aerospace Engineering*, 24(1):1–11, 2011. doi: [10.1061/\(ASCE\)AS.1943-5525.0000044](https://doi.org/10.1061/(ASCE)AS.1943-5525.0000044).
- [21] A. Elsaadany and Yi Wen-jun. Accurate trajectory prediction for typical artillery projectile. *Proceedings of the 33rd Chinese Control Conference*, pages 6368–6374, Nanjing, China, 28–30 July, 2014. doi: [10.1109/ChiCC.2014.6896037](https://doi.org/10.1109/ChiCC.2014.6896037).
- [22] R. McCoy. *Modern Exterior Ballistics*. Schiffer Publishing, Ltd., 2012.
- [23] B. Burchett and M. Costello. Model predictive lateral pulse jet control of an atmospheric rocket. *Journal of Guidance, Control, and Dynamics*, 25(5):860–867, 2002. doi: [10.2514/2.4979](https://doi.org/10.2514/2.4979).
- [24] L. Hainz III and M. Costello. Modified projectile linear theory for rapid trajectory prediction. *Journal of Guidance Control and Dynamics*, 28(5):1006–1014, 2005. doi: [10.2514/1.8027](https://doi.org/10.2514/1.8027).
- [25] F. Fresconi. Guidance and control of a projectile with reduced sensor and actuator requirements. *Journal of Guidance, Control, and Dynamics*, 34(6):1757–1766, 2011. doi: [10.2514/1.53584](https://doi.org/10.2514/1.53584).
- [26] A. Calise and H. El-Shirbiny. An analysis of aerodynamic control for direct fire spinning projectiles. *AIAA Guidance, Navigation, and Control Conference and Exhibit*, Montreal, Canada, 2001. doi: [10.2514/6.2001-4217](https://doi.org/10.2514/6.2001-4217).
- [27] Y. Zhang, M. Gao, S. Yang, and D. Fang. Optimization of trajectory correction scheme for guided mortar projectiles. *International Journal of Aerospace Engineering*, 2015:ID618458, 2015. doi: [10.1155/2015/618458](https://doi.org/10.1155/2015/618458).

- [28] W. Park, J. Yun, C.-K. Ryoo, and Y. Kim. Guidance law for a modern munition. *International Conference on Control, Automation and Systems 2010*, pages 2376–2379, Gyeonggi-do, South Korea, 27-30 October, 2010.
- [29] M. Gross and M. Costello. Impact point model predictive control of a spin-stabilized projectile with instability protection. *Proceedings of the Institution of Mechanical Engineers, Part G: Journal of Aerospace Engineering*, 228(12):2215–2225, 2014. doi: [10.1177/0954410013514743](https://doi.org/10.1177/0954410013514743).
- [30] J. Rogers. Stochastic model predictive control for guided projectiles under impact area constraints. *Journal of Dynamic Systems, Measurement, and Control*, 137(3):034503, 2015. doi: [10.1115/1.4028084](https://doi.org/10.1115/1.4028084).